

Electromagnetic anomaly in the presence of electric and chiral magnetic conductivities in relativistic heavy-ion collisions

Irfan Siddique,^{1,*} Shanshan Cao,^{1,†} Uzma Tabassam,² Mohsin Saeed,³ and Muhammad Waqas⁴

¹*Institute of Frontier and Interdisciplinary Science,
Shandong University, Qingdao, Shandong, 266237, China*

²*Department of Physics, COMSATS University Islamabad Campus, Islamabad, Park Road, 44000, Pakistan*

³*Department of Physics, University of the Punjab,
Quaid-e-Azam Campus, Lahore, 54590, Pakistan*

⁴*School of Nuclear Science and Technology, University of Chinese Academy of Sciences, Beijing, 100049, China*

We study the spacetime evolution of electric (\mathbf{E}) and magnetic (\mathbf{B}) fields along with the electromagnetic anomaly ($\mathbf{E} \cdot \mathbf{B}$) in the presence of electric (σ) and chiral magnetic (σ_χ) conductivities in Au+Au collisions at $\sqrt{s_{NN}} = 200$ GeV. By comparing to the Lienard-Wiechert solutions with zero conductivities, we observe a symmetry breaking of the electromagnetic field in a conducting medium with respect to the reaction plane. The decay of the field is also significantly decelerated after the conductivities are introduced. Similar effects are also found for the dipole structure of $\mathbf{E} \cdot \mathbf{B}$ as well as the quadrupole structure of $(\mathbf{E} \cdot \mathbf{B})\mathbf{B}$, which may finally affect the charge separation of the elliptic flow coefficient of hadrons observed in high-energy nuclear collisions.

I. INTRODUCTION

The high-speed movement of charged nuclei in non-central relativistic heavy-ion collisions can produce strong electromagnetic field. Its magnitude can be estimated via $eB \sim \gamma v Z e^2 / R_A^2$, whose peak value can reach the order of 10^{18} Gauss in Au+Au collisions at the BNL Relativistic Heavy-Ion Collider (RHIC), and 10^{19} Gauss in Pb+Pb collisions at the CERN Large Hadron Collider (LHC) [1–4]. This provides a unique environment to investigate properties of nuclear matter under extreme electromagnetic field, such as the anomalous transport effects in the quark-gluon plasma (QGP) produced by the energetic nuclear collisions [5–10]. The electromagnetic field can also cause separation of particles with opposite charges, as reflected by the charge-odd directed flow coefficient found in both theoretical calculations [11–17] and experimental measurements [18, 19], although a precise agreement between theory and experiment is still an ongoing effort.

With the presence of an external electric field \mathbf{E} , one would expect a vector current induced in a conducting matter according to the Ohm's law,

$$\mathbf{j}_V = \sigma \mathbf{E}, \quad (1)$$

with σ being the electric conductivity and \mathbf{j}_V being the electric current. Meanwhile, inside a plasma composed of chiral fermions, vector current j_V^μ and axial current j_A^μ can also be induced by magnetic field \mathbf{B} . If chiral anomaly, or a nonzero axial chiral charge potential μ_A , exists, a vector current $\mathbf{j}_V = \langle \bar{\psi} \gamma^i \psi \rangle$ will be induced by the imbalance between left and right handed quarks as [20–22]:

$$\mathbf{j}_V^{\text{CME}} = \sigma_5 \mu_A \mathbf{B}, \quad (2)$$

where σ_5 is known as the chiral magnetic conductivity given by $\sigma_5 \simeq e N_c / 2\pi^2$ with N_c being the number of colors. This is known as the chiral magnetic effect (CME). With the mass term included, the axial anomaly equation reads [23, 24],

$$\partial_\mu j_5^\mu = 2im\bar{\psi}\gamma^5\psi - \frac{e^2}{16\pi^2}\epsilon^{\mu\nu\rho\sigma}F_{\mu\nu}F_{\rho\sigma} - \frac{g^2}{16\pi^2}\text{tr}\epsilon^{\mu\nu\rho\sigma}G_{\mu\nu}G_{\rho\sigma}, \quad (3)$$

from which one can observe three terms of contributions to the axial charge. The first term on the right hand side comes from the finite quark mass originated from the chiral symmetry breaking, while the second and third terms correspond to the QED and QCD anomalies respectively. The QED anomaly, usually represented by $\mathbf{E} \cdot \mathbf{B}$, will be the main focus of this work.

Similarly, a nonzero vector chemical potential μ_A would induce an axial current $\mathbf{j}_A = \langle \bar{\psi} \gamma^i \gamma^5 \psi \rangle$ in the presence of the external \mathbf{B} field [25, 26]:

$$\mathbf{j}_A^{\text{CSE}} = \sigma_5 \mu_V \mathbf{B}, \quad (4)$$

which causes the axial charge separation along the \mathbf{B} and is known as the chiral separation effect (CSE).

Chiral magnetic and chiral separation effects have been investigated within various approaches, such as hydrodynamics, kinetic theory, holographic QCD and lattice QCD [27–33]. It has been proposed that the nonzero vector and axial charges can mutually induce each other, leading to a collective excitation in the QGP known as the chiral magnetic wave (CMW) [21, 34, 35]. The charge quadrupole structure associated with this CMW can further result in different elliptic flow coefficients (v_2) between positive and negative charged particles [22, 36], as observed by the STAR experiment [37]. Nevertheless, it has been suggested in Ref. [38] that even without the formation of CMW, the dipole shape of the $\mathbf{E} \cdot \mathbf{B}$ distribution in the transverse plane can already generate

* irfansiddique@sdu.edu.cn

† shanshan.cao@sdu.edu.cn

an electric quadrupole moment when being coupled to the magnetic field \mathbf{B} . This provides an alternative direction for understanding the v_2 separation between opposite charges, considering the negative result on the recent search for the CME at RHIC [39]. Moreover, this novel mechanism does not need a finite baryon density (μ_V) to drive the charge separation of v_2 , therefore may lead to different beam energy dependence of this charge separation, which can be further tested by the beam energy scan program at RHIC. The space-averaged electromagnetic field and electromagnetic anomaly weighted by energy density have been further investigated in Ref. [40].

In this work, we extend these previous studies [38, 40] on the spatial distribution of $\mathbf{E} \cdot \mathbf{B}$ to a more realistic nuclear medium that includes both electric and chiral magnetic conductivities. It has been found that the decay of the electromagnetic field can be significantly decelerated when conductivities are introduced [11, 41–46]. Symmetry breaking has also been suggested for the field with respect to the reaction plane after including the conductivities [43]. We will follow Ref. [43] to further investigate the time evolution of the spatial distribution of the electromagnetic field in the presence of electric and chiral magnetic conductivities. In particular, effects on the dipole structure of the electromagnetic anomaly and the electric quadrupole pattern will be discussed in detail.

This work will be organized as follows. We will first provide a brief review on the solution of the electromagnetic field in both conducting and non-conducting media in Sec. II. Numerical results of the spacetime evolution of the electromagnetic field will be presented in Sec. III, and compared between with and without including electric and chiral magnetic conductivities. In Sec. IV, we will discuss effects of conductivities on the electromagnetic anomaly and the electric quadrupole moment. A summary and outlook will be presented in Sec. V.

II. CALCULATION OF ELECTROMAGNETIC FIELD

A: Non-conducting System ($\sigma = \sigma_\chi = 0$)

For a non-conducting system, or vacuum, where both electric and chiral magnetic conductivities are zero ($\sigma = \sigma_\chi = 0$), we evaluate the electromagnetic field according to the Lienard-Wiechert potential [1, 47] as

$$\mathbf{E}(t, \mathbf{x}) = \frac{e}{4\pi} \sum_n \frac{(1 - v_n^2) \mathbf{R}_n}{(\mathbf{R}_n^2 - (\mathbf{R}_n \times \mathbf{v}_n)^2)^{3/2}}, \quad (5)$$

$$\mathbf{B}(t, \mathbf{x}) = \frac{e}{4\pi} \sum_n \frac{(1 - v_n^2) (\mathbf{v}_n \times \mathbf{R}_n)}{(\mathbf{R}_n^2 - (\mathbf{R}_n \times \mathbf{v}_n)^2)^{3/2}}, \quad (6)$$

where $\mathbf{R}_n = \mathbf{x} - \mathbf{x}_n$ is the relative position vector between the field point \mathbf{x} under discussion and the source point

\mathbf{x}_n , and \mathbf{x}_n and \mathbf{v}_n are respectively the position and velocity of the n -th proton in the colliding nuclei at the current time t . Note that the above equations are valid when each source charge is traveling with a constant velocity. Otherwise, the original form of the Lienard-Wiechert fields [2] using the retarded time should be applied.

B: Conducting System ($\sigma \neq 0, \sigma_\chi \neq 0$)

The QGP matter produced in heavy-ion collisions is a conducting medium. The in-medium electromagnetic field can be solved using the Maxwell equations with both electric (σ) and chiral magnetic (σ_χ) conductivities included:

$$\nabla \cdot \mathbf{F} = \begin{cases} \rho_{\text{ext}}/\epsilon & \rightarrow \mathbf{E} \\ 0 & \rightarrow \mathbf{B} \end{cases}, \quad (7)$$

$$\nabla \times \mathbf{F} = \begin{cases} -\partial_t \mathbf{B} & \rightarrow \mathbf{E} \\ \partial_t \mathbf{E} + \mathbf{J}_{\text{ext}} + \sigma \mathbf{E} + \sigma_\chi \mathbf{B} & \rightarrow \mathbf{B} \end{cases}, \quad (8)$$

where ρ_{ext} and \mathbf{J}_{ext} are external charge and current densities, and \mathbf{F} denotes either electric (\mathbf{E}) or magnetic (\mathbf{B}) field. Considering that all source charges propagate along the z -axis, one can obtain the following algebraic solutions of the electromagnetic field using the Green's function method in the cylindrical coordinates [43]:

$$\begin{aligned} B_\phi(t, \mathbf{x}) &= \frac{Q}{4\pi} \frac{v\gamma x_T}{\Delta^{3/2}} \left(1 + \frac{\sigma v\gamma}{2} \sqrt{\Delta}\right) e^A, \\ B_r(t, \mathbf{x}) &= -\sigma_\chi \frac{Q}{8\pi} \frac{v\gamma^2 x_T}{\Delta^{3/2}} e^A \left[\gamma(vt - z) + A\sqrt{\Delta}\right], \\ B_z(t, \mathbf{x}) &= \sigma_\chi \frac{Q}{8\pi} \frac{v\gamma}{\Delta^{3/2}} e^A \left[\Delta \left(1 - \frac{\sigma v\gamma}{2} \sqrt{\Delta}\right) \right. \\ &\quad \left. + \gamma^2 (vt - z)^2 \left(1 + \frac{\sigma v\gamma}{2} \sqrt{\Delta}\right)\right], \end{aligned} \quad (9)$$

in which Δ and A are defined as $\Delta \equiv \gamma^2 (vt - z)^2 + x_T^2$ and $A \equiv (\sigma v\gamma/2) \left[\gamma(vt - z) - \sqrt{\Delta}\right]$, with x_T being the magnitude of the transverse coordinate $x_T = \sqrt{x^2 + y^2}$; and

$$\begin{aligned} E_\phi(t, \mathbf{x}) &= \sigma_\chi \frac{Q}{8\pi} \frac{v^2 \gamma^2 x_T}{\Delta^{3/2}} e^A \left[\gamma(vt - z) + A\sqrt{\Delta}\right], \\ E_r(t, \mathbf{x}) &= \frac{Q}{4\pi} e^A \left\{ \frac{\gamma x_T}{\Delta^{3/2}} \left(1 + \frac{\sigma v\gamma}{2} \sqrt{\Delta}\right) \right. \\ &\quad \left. - \frac{\sigma}{v x_T} e^{-\sigma(t-z/v)} \left[1 + \frac{\gamma(vt - z)}{\sqrt{\Delta}}\right] \right\}, \\ E_z(t, \mathbf{x}) &= \frac{Q}{4\pi} \left\{ -\frac{e^A}{\Delta^{3/2}} \left[\gamma(vt - z) + A\sqrt{\Delta} + \frac{\sigma\gamma}{v} \Delta\right] \right. \\ &\quad \left. + \frac{\sigma^2}{v^2} e^{-\sigma(t-z/v)} \Gamma(0, -A) \right\}, \end{aligned} \quad (10)$$

with $\Gamma(0, -A)$ being the incomplete gamma function defined as $\Gamma(a, z) = \int_z^\infty t^{a-1} \exp(-t) dt$. One may verify

that Eqs. (9) and (10) above return to the previous Lienard-Wiechert solution with vanishing σ and σ_χ .

In this work, we use the Monte-Carlo (MC) Glauber model developed by the PHOBOS Collaboration [48] to calculate the spatial distribution of the source charges. A two-step calculation is performed in this model. First, for a given impact parameter b , the centers of projectile and target nuclei are located at $x = \pm b/2$ with the impact parameter defined in the x -direction and the beams in the z -direction. The positions of nucleons in the two nuclei are determined stochastically. The Woods-Saxon distribution is taken for the density profile of nucleons in each nucleus

$$\rho(r, \theta) = \frac{\rho_0}{1 + \exp\left[\frac{r - R(\theta)}{d}\right]} \left[1 + w \frac{r^2}{R(\theta)^2}\right], \quad (11)$$

where ρ_0 denotes the nuclear density at the nucleus center, d is the surface thickness parameter, and $R(\theta) = R_0[1 + \beta_2 Y_{20}(\theta) + \beta_4 Y_{40}(\theta)]$ is the nuclear radius in which $Y_{nl}(\theta)$ are spherical harmonic functions. Here, the parameters β_2 , β_4 and w determine the deviation from a spherical nucleus. These nucleons are then assumed to propagate along straight trajectories (in $\pm z$ directions). For each pair of nucleons, one from projectile and one from target, a collision between them takes place if their distance d (in the transverse plane) satisfies $d \leq \sqrt{\sigma_{\text{inel}}^{\text{NN}}/\pi}$, where $\sigma_{\text{inel}}^{\text{NN}}$ is the inelastic cross section of nucleon-nucleon collisions. Those nucleons that participate in collisions are labelled as “participants” while those that do not participate in collisions are labelled as “spectators”.

In this work, we use $\sigma_{\text{inel}}^{\text{NN}} = 42 \text{ mb}$, $\rho_0 = 0.17 \text{ fm}^{-3}$, $R = 6.38 \text{ fm}$, $d = 0.535 \text{ fm}$ and $w = 0$ for Au-Au collisions at $\sqrt{s_{\text{NN}}} = 200 \text{ GeV}$ at RHIC. We define the initial time ($t = 0$) as the moment when the two oppositely moving nuclei collide. In Fig. 1, we illustrate our initial charge distribution based on this MC Glauber approach, left for the view on the transverse plane, and right for the view on the reaction plane. Purple and green dots represent participant nucleons from the two colliding nuclei, while blue and red represent spectators that do not participate in inelastic scatterings. For each nucleon, we use the probability Z/A (79/197 for Au nucleus) to determine whether it is a proton that contributes to the electromagnetic field we discuss. Protons in both participants and spectators are taken into account for evaluating the electromagnetic field. Minor difference has been found between considering only spectators and all nucleons. For instance, for $b = 10 \text{ fm}$, protons in spectators alone yield about 6% smaller B_y compared to protons in the whole nucleus. For calculating the electromagnetic field in the rest of this study, we average over 50,000 MC Glauber events for each impact parameter setup to obtain a smooth geometric distribution of the source charges.

III. SPATIAL DISTRIBUTIONS OF ELECTROMAGNETIC FIELDS

In this section we present our numerical results on the spatial distribution of the electric and magnetic fields, compared between zero and finite electric (σ) and chiral magnetic (σ_χ) conductivity cases. Based on the previous discussions in Sec. II, the MC Glauber model is used to obtain the spacetime evolution profile of electric charges for Au+Au collisions at $\sqrt{s_{\text{NN}}} = 200 \text{ GeV}$ with different impact parameters, the Maxwell equations are solved for the electromagnetic fields with finite σ and σ_χ , while the Lienard-Wiechert solution is taken for the case of $\sigma = \sigma_\chi = 0$.

Shown in Figs. 2 - 5 are the spatial distributions of eE_x , eE_y , eB_x , eB_y respectively in Au+Au collisions at $\sqrt{s_{\text{NN}}} = 200 \text{ GeV}$. In each figure, we present the Lienard-Wiechert solution for vacuum in the first row and results for finite conductivities in the second row. Here the conductivities are taken as $\sigma = 5.8 \text{ MeV}$ and $\sigma_\chi = 1.5 \text{ MeV}$ as used in Ref. [43]. Note that the value of $\sigma = 5.8 \text{ MeV}$ is consistent with the lattice QCD result around the top temperature of the QGP at RHIC [49, 50], which is expected to decrease together with the medium temperature as the QGP expands. In addition, there is no direct guidance of how to choose the value of σ_χ yet. Since the analytical solution of the electromagnetic field – Eqs. (9) and (10) – is obtained in the limit of $\sigma_\chi \ll \sigma$ in Ref. [43], we take the value assigned in this original work. In the present study, we will only focus on investigating the effects of the electric and chiral magnetic conductivities with the given values above. Constraints on these values will be explored in a follow-up study where we connect electromagnetic effects to experimental observables. In each row of the figures, two snapshots of time evolution are presented. For the vacuum cases, due to the rapid decay of the electromagnetic field, we present results for $t = 0.1 \text{ fm}/c$ and $0.3 \text{ fm}/c$. On the other hand, $t = 0.1 \text{ fm}/c$ and $1.1 \text{ fm}/c$ are presented for the finite conductivity cases in which the decay speed is much slower. And for each snapshot, results for two impact parameters, $b = 4 \text{ fm}$ and 8 fm are shown.

For the electric field presented in Figs. 2 and 3, one observes its magnitude decreases as the impact parameter increases. It is maximized at the most central collisions, as has been shown in Ref. [38]. As time evolves, the electric field spreads out in space with a decreasing magnitude. Comparing between the upper and lower panels, one can observe the electric field decays much slower when the conductivities σ and σ_χ are present. It is interesting to note that when $\sigma = \sigma_\chi = 0$, the spatial distributions of both $|E_x|$ and $|E_y|$ appear symmetric with respect to both $x = 0$ and $y = 0$ axes. However, for finite conductivities, these distributions are only symmetric about the $x = 0$ axis but asymmetric about $y = 0$. This could be understood with the non-zero azimuthal component E_ϕ with the presence of σ_χ . Similar to the illustration provided in Ref. [43], if one assumes one pro-

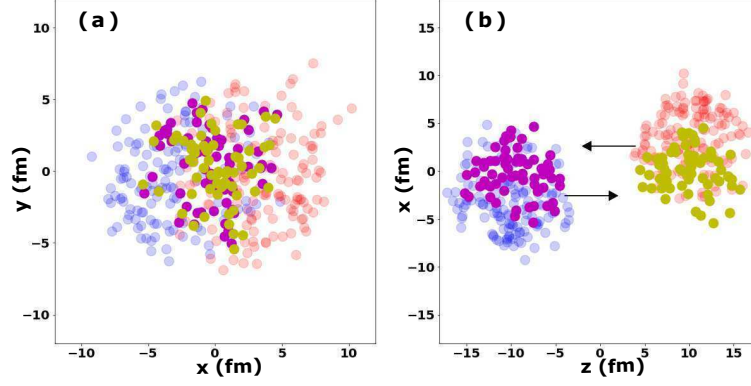


Figure 1. (Color online) Initial geometry of a Au+Au collision event generated by the MC Glauber model for $b = 10$ fm and $\sqrt{s_{NN}} = 200$ GeV, left for the view on the transverse plane and right for the view on the reaction plane.

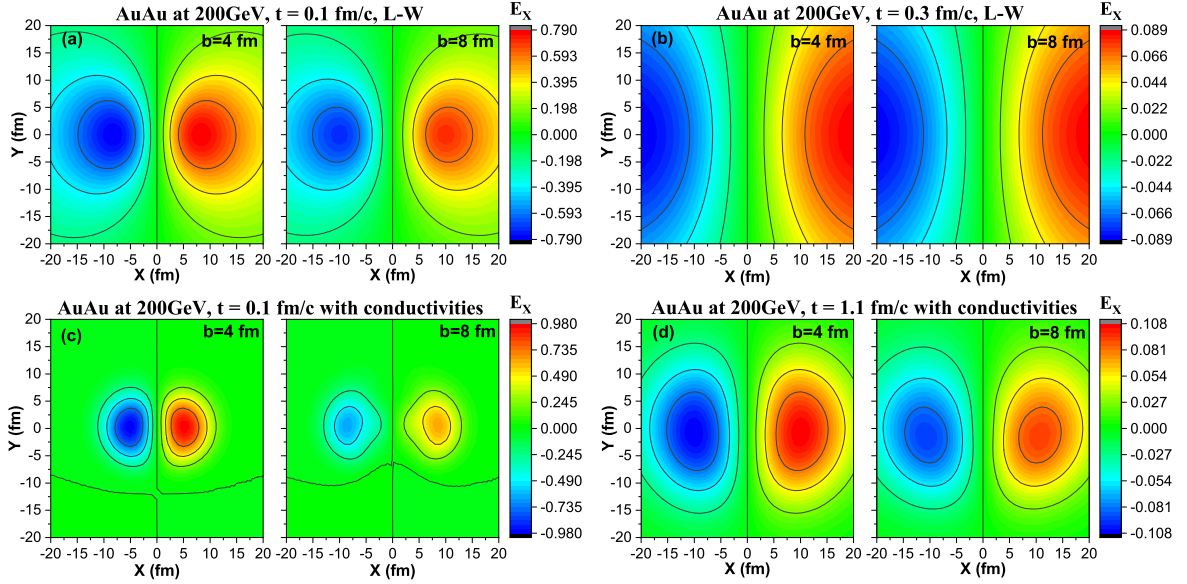


Figure 2. (Color online) The spatial distributions of eE_x (in the unit of m_π^2) in 200 AGeV Au+Au collisions, compared between zero *vs.* finite conductivities, different impact parameters and evolution times.

ton travels in $-\hat{z}$ at $(-a, 0, 0)$ while another travels in $+\hat{z}$ at $(a, 0, 0)$, the E_r components they generate according to Eq. (10) will contribute to the same sign of E_x at two symmetric locations with respect to the $y = 0$ axis, e.g. $(b, c, 0)$ and $(b, -c, 0)$, while opposite sign of E_y at these two locations. To the contrary, the E_ϕ components from the two moving charges will generate opposite sign of E_x while same sign of E_y at the two locations above. As a result, the finite E_ϕ breaks the original symmetry of $E_x(y) = E_x(-y)$ and $E_y(y) = -E_y(-y)$ at zero conductivities.

Some similar features can be observed in Figs. 4 and 5 for the spatial distributions of the magnetic field, such as the slower decay of $|B_x|$ and $|B_y|$ and their spread into space after finite σ and σ_χ are included, as well as their broken symmetry with respect to the reaction plane when finite conductivities are present. However, differ-

ent from the electric field, it is the radial component B_r in Eq. (9), determined by σ_χ , that breaks the original $B_x(y) = -B_x(-y)$ and $B_y(y) = B_y(-y)$ symmetry at zero conductivities. In addition, different patterns of the spatial distribution can also be found between electric and magnetic fields. And opposite to the electric field, the magnetic field increases as the impact parameter increases.

In Fig. 6, we present the spatial distributions of the electric (upper panels) and magnetic (lower panels) field in the longitudinal direction. Unlike the transverse components, even in the presence of the electric and chiral magnetic conductivities, E_z and B_z distributions still appear symmetric about both $x = 0$ and $y = 0$ axes. This could be understood with the B_z and E_z components directly given by Eqs. (9) and (10). Two protons moving along $\pm\hat{z}$ at $(\pm a, 0, 0)$ yield $F_z(y) = F_z(-y)$ and

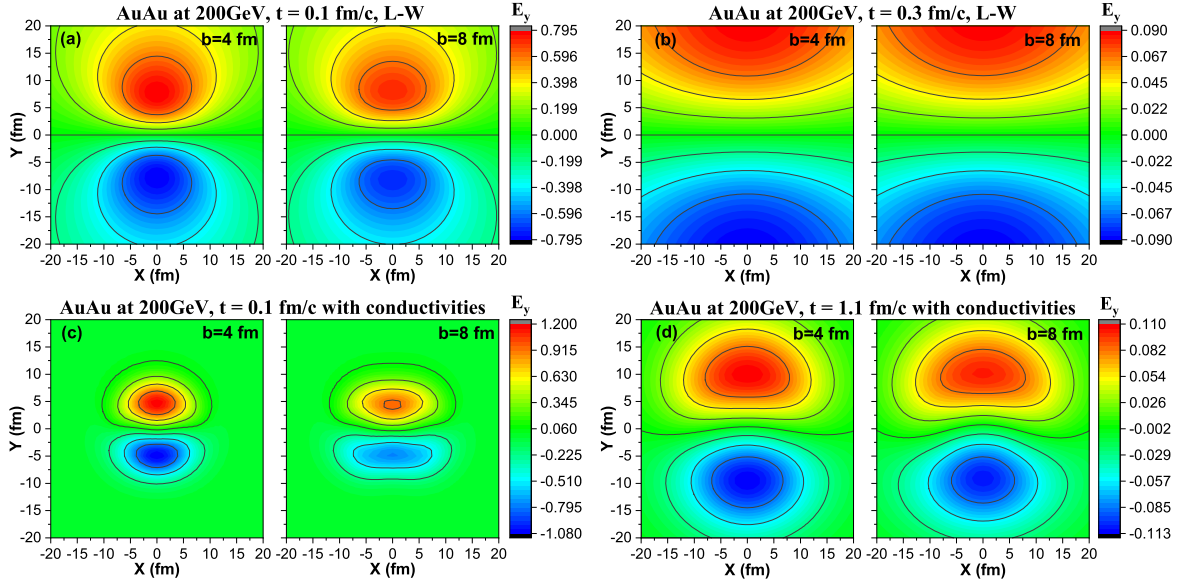


Figure 3. (Color online) The spatial distributions of eE_y (in the unit of m_π^2) in 200 AGeV Au+Au collisions, compared between zero *vs.* finite conductivities, different impact parameters and evolution times.

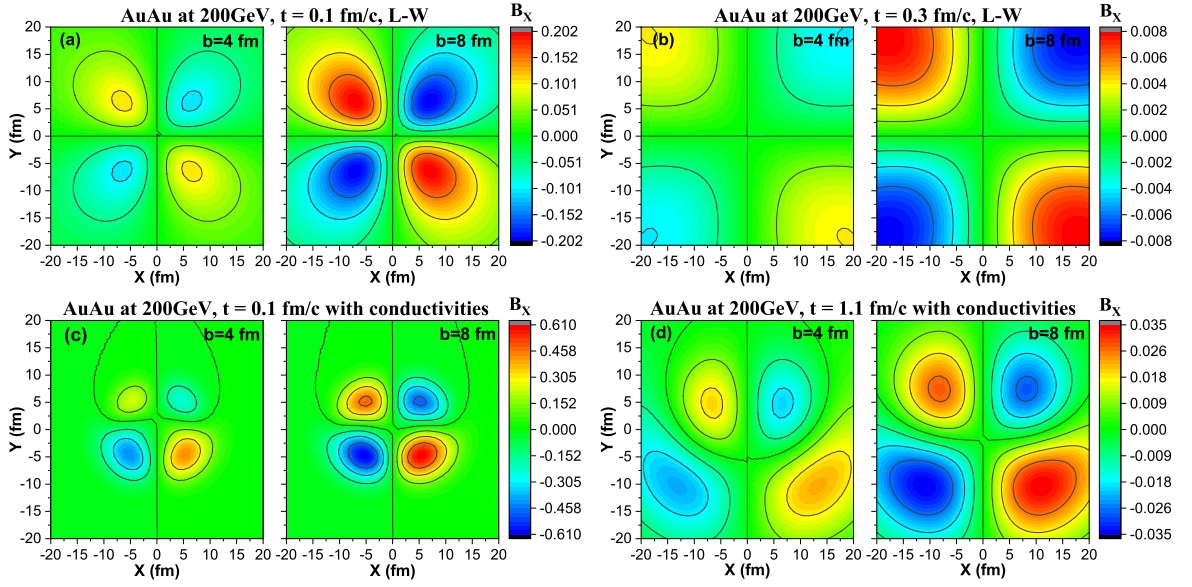


Figure 4. (Color online) The spatial distributions of eB_x (in the unit of m_π^2) in 200 AGeV Au+Au collisions, compared between zero *vs.* finite conductivities, different impact parameters and evolution times.

$F_z(x) = -F_z(-x)$, with F_z for both B_z and E_z . And compared to their corresponding transverse components, the magnitudes of electric and magnetic fields are much smaller in the longitudinal direction, as has been suggested in Refs. [1, 2, 51].

For a better illustration of the field configuration, we present the two-dimensional vector fields of \mathbf{E}_T (upper panels) and \mathbf{B}_T (lower panels) in the transverse plane at $z = 0$ in Fig. 7, in which the contour plots are for the magnitude of $|\mathbf{E}_T|$ and $|\mathbf{B}_T|$. One can observe a clear broken symmetry of both $|\mathbf{E}_T|$ and $|\mathbf{B}_T|$ about the $y = 0$

axis after finite conductivities are introduced. The breaking appears stronger for the magnetic field than the electric field. Moreover, as shown by the vector field, one can clearly see the zero electric field near the origin $(0, 0, 0)$, while a finite magnetic field along $-\hat{y}$. Note that without conductivity, the magnetic field follows the $-\hat{y}$ direction along the $x = 0$ axis. However, its direction changes after conductivities are introduced, especially when the position is away from the origin. This would affect the inner product between electric and magnetic fields, as will be discussed in the following section.

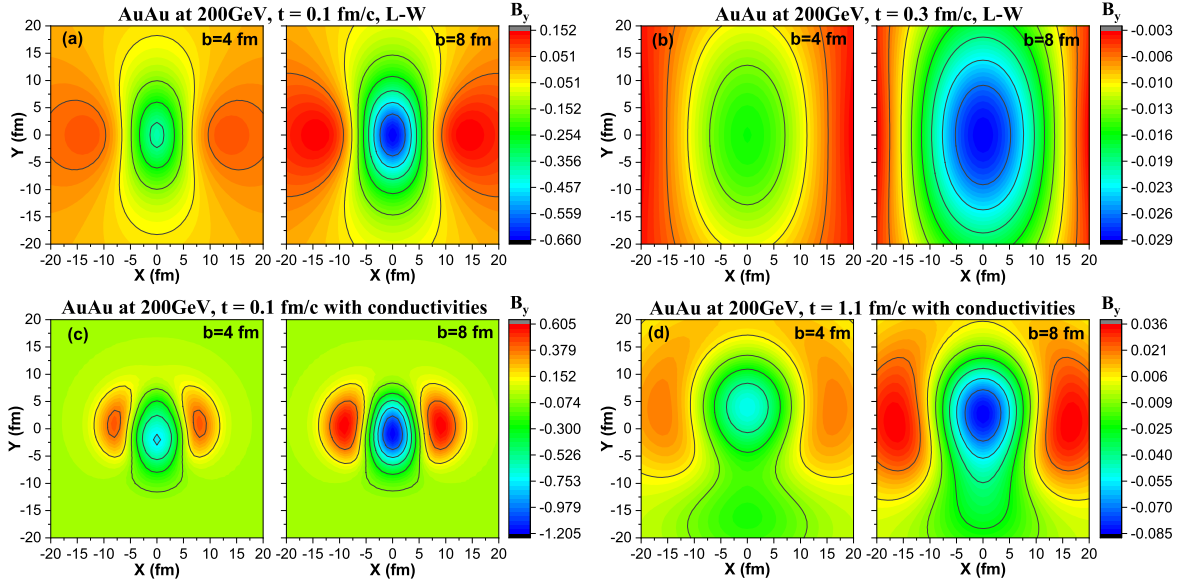


Figure 5. (Color online) The spatial distributions of eB_y (in the unit of m_π^2) in 200 AGeV Au+Au collisions, compared between zero *vs.* finite conductivities, different impact parameters and evolution times.

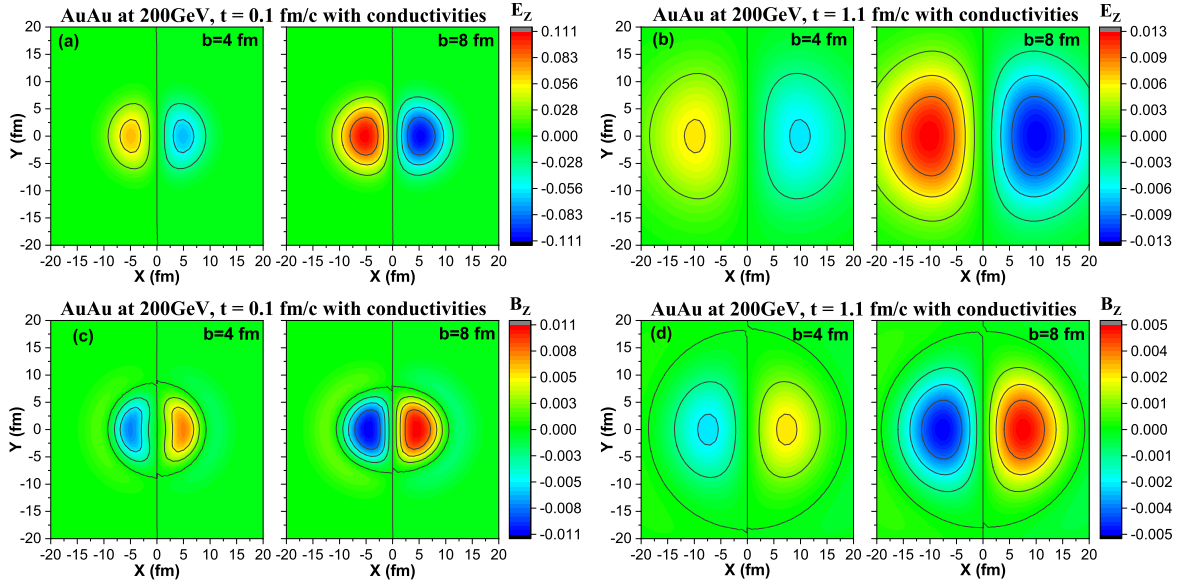


Figure 6. (Color online) The spatial distributions of eE_z (upper panels) and eB_z (lower panels) (in the unit of m_π^2) in 200 AGeV Au+Au collisions in the presence of finite conductivities, compared between different impact parameters and evolution times.

IV. SPATIAL DISTRIBUTIONS OF $\mathbf{E} \cdot \mathbf{B}$

With the separate results of \mathbf{E} and \mathbf{B} fields above, we further investigate the spatial distribution of their inner product ($\mathbf{E} \cdot \mathbf{B} = E_x B_x + E_y B_y + E_z B_z$), which is directly related to the generation of the electric quadrupole moment. We keep contributions from both transverse and longitudinal components for the inner product for completeness, though one may also neglect the longitudinal part [38] due to its relatively small contribution.

In Fig. 8, we first present the spatial distribution of the

angle between electric and magnetic fields in the transverse plane. For the most central collisions ($b = 0$), one may consider orthogonality between \mathbf{E}_T and \mathbf{B}_T due to the vanishing magnitude of the magnetic field. At finite impact parameter, \mathbf{E}_T and \mathbf{B}_T are orthogonal to each other around the $y = 0$ axis, but appear parallel or anti-parallel around the $x = 0$ axis. In vacuum, one expects to see anti-parallel alignment in the $y > 0$ half plane while parallel alignment in the $y < 0$ half plane. However, after conductivities are introduced, parallel configuration can also be observed in the $y > 0$ half plane. This is mainly

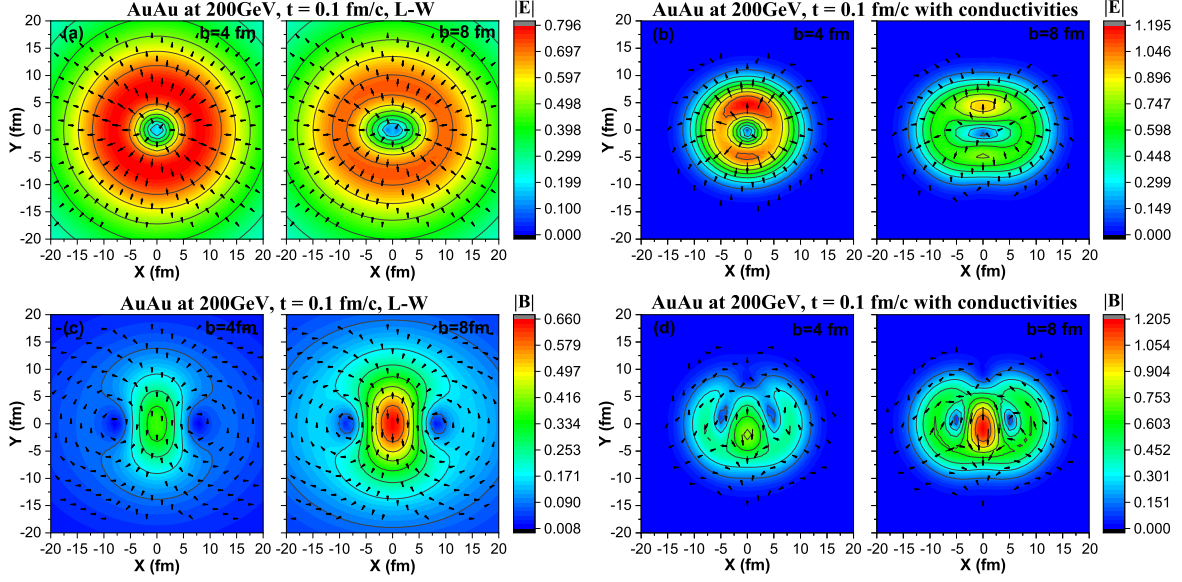


Figure 7. (Color online) The spatial distributions of the magnitude of $e\mathbf{E}_T$ (upper panels) and $e\mathbf{B}_T$ (lower panels) (in the unit of m_π^2), together with their two-dimensional vector fields in 200 AGeV Au+Au collisions at $t = 0.1$ fm/c, compared between zero *vs.* finite conductivities and different impact parameters.

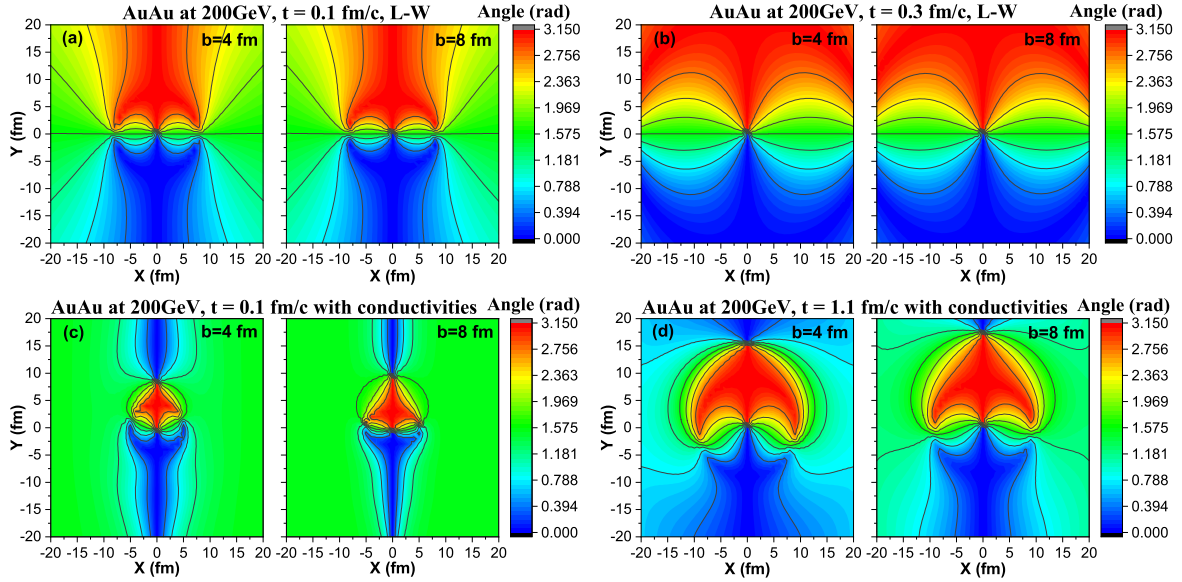


Figure 8. (Color online) The spatial distributions of the angle between \mathbf{E}_T and \mathbf{B}_T in 200 AGeV Au+Au collisions, compared between zero *vs.* finite conductivities, different impact parameters and evolution times.

due to the direction flip of the magnetic field, as has been discussed in Fig. 7. As time evolves, the pattern of these angular distributions expand outwards in the transverse plane. A faster expansion is seen in vacuum than in a conducting medium.

Shown in Fig. 9 is the distribution of $\mathbf{E} \cdot \mathbf{B}$, compared between zero *vs.* finite conductivities, and different impact parameters and evolution times. One naturally expect to see zero values for the most central collisions, while finite value for peripheral collisions. Symmetric dis-

tributions are observed with respect to the reaction plane (or the $y = 0$ axis) for the Lienard-Wiechert solution, as presented in Ref. [38]. However, these distributions become asymmetric after finite σ and σ_χ are included. Despite the asymmetric distribution, one can still observe a dipole structure of $\mathbf{E} \cdot \mathbf{B}$, i.e., opposite signs in the $y > 0$ and $y < 0$ half planes. The generation of this dipole structure can be understood with the angular distributions in Fig. 8, where the electric and magnetic fields are generally parallel to each other in the $y < 0$ half plane

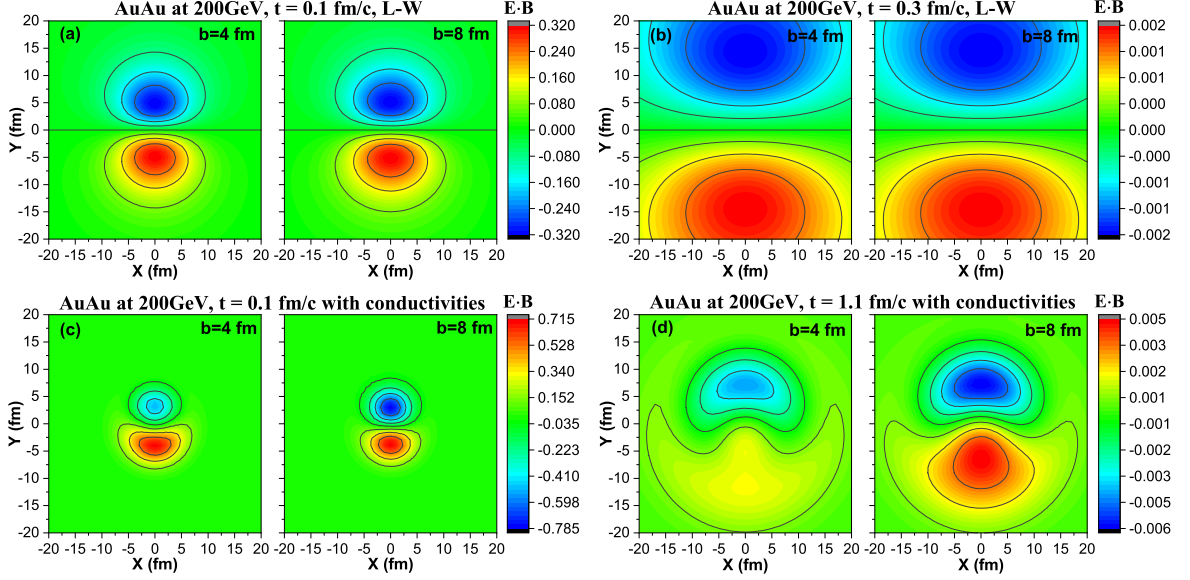


Figure 9. (Color online) The spatial distributions of $e^2 \mathbf{E} \cdot \mathbf{B}$ (in the unit of m_π^4) in 200 AGeV Au+Au collisions, compared between zero *vs.* finite conductivities, different impact parameters and evolution times.

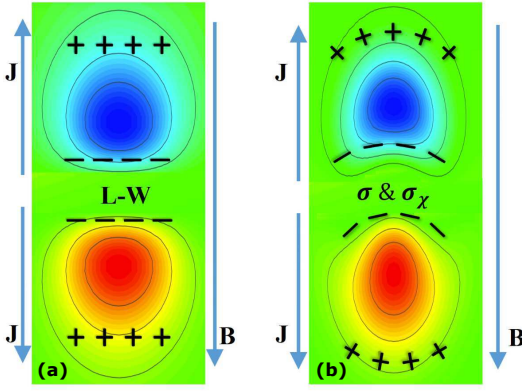


Figure 10. (Color online) Generation of an electric quadrupole moment from coupling between $\mathbf{E} \cdot \mathbf{B}$ and \mathbf{B} in non-central 200 AGeV Au+Au collisions, compared between zero (left panel) and finite (right panel) conductivities.

while anti-parallel for $y > 0$. Although parallel alignment is also seen in the $y > 0$ region, the small magnitude of the fields at those positions far away from the origin prevents the breaking of the overall dipole structure.

Non-zero $\mathbf{E} \cdot \mathbf{B}$ implies non-zero μ_A . According to Eq. (2), the CME current can be induced in the presence of a magnetic field. As illustrated in Fig. 10, with a magnetic field aligning towards $-\hat{y}$, a negative $\mathbf{E} \cdot \mathbf{B}$ in the $y > 0$ region induces a current \mathbf{J} towards $+\hat{y}$, while a positive $\mathbf{E} \cdot \mathbf{B}$ in the $y < 0$ region makes \mathbf{J} along $-\hat{y}$, generating an electric quadrupole moment in the end. This would guide positive charges into the out-of-plane direction of heavy-ion collisions, while negative charges into the in-plane direction, giving rise to the charge separa-

tion of hadron v_2 even without the formation of CMW. Taking into account the finite σ and σ_χ affects the direction of the local CME current, resulting in a quantitatively different electric quadrupole moment compared to the vacuum scenario, although the qualitative picture is still consistent with the findings proposed in Ref. [38].

To further investigate how the conductivities quantitatively affect the electric quadrupole moment, in Fig. 11 we compare the participant number (N_{part}) dependence of $\mathbf{E} \cdot \mathbf{B}$ between the Lienard-Wiechert solution and the solution of the Maxwell equations with finite conductivities. Results are shown for different locations at the initial time. In the upper panel, we observe that at $(0, -4 \text{ fm}, 0)$, $\mathbf{E} \cdot \mathbf{B}$ from with and without conductivities share similar shape of the N_{part} dependence. It first increases and then decreases as N_{part} increases, since the electric field is small at large impact parameter (small N_{part}) while the magnetic field is small at small impact parameter (large N_{part}). On the other hand, the magnitude of $\mathbf{E} \cdot \mathbf{B}$ with conductivities is about 9 times smaller than that without conductivities at the initial time. In addition, while the absolute value of $\mathbf{E} \cdot \mathbf{B}$ with zero conductivities are symmetric at $(0, -4 \text{ fm}, 0)$ and $(0, +4 \text{ fm}, 0)$ (the black and red curves overlap each other), such symmetry is broken (between the blue and green curves) after finite conductivities are introduced. Similar findings have also been confirmed in the lower panel for the locations of $(0, \pm 6 \text{ fm}, 0)$.

Shown in Fig. 12 is the zone averaged $|\mathbf{E} \cdot \mathbf{B}|$ as a function of the participant number at the initial time. The average is conducted over the geometric overlapping region between the two colliding nuclei, i.e., region that simultaneously satisfies $(x - b/2)^2 + y^2 < r_A^2$ and $(x + b/2)^2 + y^2 < r_A^2$, with b being the impact parameter and

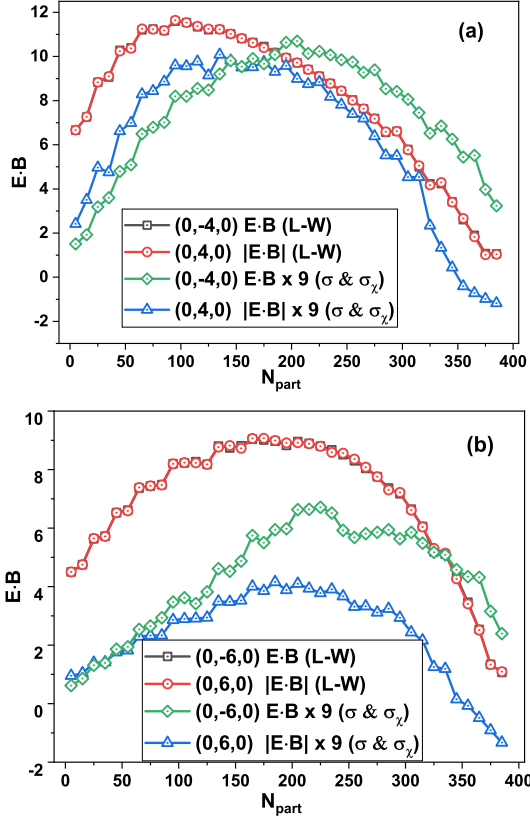


Figure 11. (Color online) The value of $e^2 \mathbf{E} \cdot \mathbf{B}$ (in the unit of m_π^4) as a function of N_{part} at the initial time, and positions of $\mathbf{r} = (0, \pm 4 \text{ fm}, 0)$ (upper panel) and $\mathbf{r} = (0, \pm 6 \text{ fm}, 0)$ (lower panel) in 200 AGeV Au+Au collisions, compared between zero and finite conductivities.

r_A being the nucleus radius parameter taken as 6.5 fm here. Uncertainties from taking different r_A values and applying different average schemes have been discussed in Ref. [38] and found small. In the upper panel of Fig. 12, we first follow Ref. [38] to present the zone averaged value of $\mathbf{E} \cdot \mathbf{B}$ in the $y < 0$ half plane. Similar to previous results at a specific location, the zone averaged $\mathbf{E} \cdot \mathbf{B}$ share a similar shape with respect to N_{part} between zero and finite conductivities, although the magnitude at the initial time becomes much smaller after conductivities are included.

Since the electromagnetic field in a conducting medium is asymmetric about the reaction plane, averaging in the $y < 0$ half plane is no longer a good representation of the dipole structure of $\mathbf{E} \cdot \mathbf{B}$ over the whole overlapping region. Therefore, in the lower panel of Fig. 12, we compare different average schemes for the finite conductivity scenario. Visible difference can be observed between averaging $\mathbf{E} \cdot \mathbf{B}$ over the $y < 0$ half plane (black curve) and averaging $|\mathbf{E} \cdot \mathbf{B}|$ over the whole overlapping region (red curve). In this lower panel, the shape of the average $|\mathbf{E} \cdot \mathbf{B}|$ is also compared to the slope parameter of the charge separation of the hadron v_2 measured by the STAR Collaboration [37] (purple), as proposed in Ref. [38]. The slope

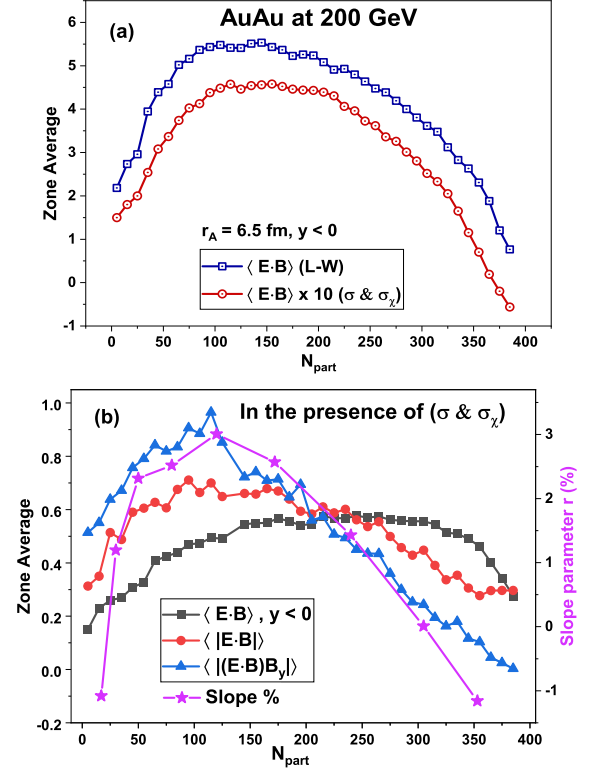


Figure 12. (Color online) The zone-averaged $|\mathbf{E} \cdot \mathbf{B}|$ (in the unit of m_π^4) and $|(\mathbf{E} \cdot \mathbf{B})B_y|$ (in the unit of m_π^6) in the geometric overlapping region between colliding nuclei at the initial time of 200 AGeV Au+Au collisions, as a function of N_{part} , compared between zero and finite conductivities (upper panel), and between different average schemes and the slope parameter r measured by the STAR Collaboration [37] (lower panel).

parameter r , defined via $v_2(\pi^\pm) = v_2^{\text{base}}(\pi^\pm) \mp r A_{\text{ch}}/2$ with the charge asymmetry of the collision system given by $A_{\text{ch}} = (N_+ - N_-)/(N_+ + N_-)$, quantifies the different v_2 between π^+ and π^- . As shown in the figure, the average $|\mathbf{E} \cdot \mathbf{B}|$ shares a similar N_{part} dependence to the measured r parameter, implying the QED anomaly ($\mathbf{E} \cdot \mathbf{B}$) could be a possible source for the separation of v_2 between positive and negative charges. Since the electric quadrupole moment is a more direct cause of the charge separation of v_2 , we also present the zone average of $|(\mathbf{E} \cdot \mathbf{B})B_y|$ in the figure (blue curve). Indeed, a better qualitative agreement is obtained with the shape of the measured r parameter. Nevertheless, a quantitative description of the experimental data would require coupling the electromagnetic field with the QGP expansion (e.g. the hydrodynamic model). This is beyond the scope of the present work and will be left for a future exploration.

In the end, we study the time evolution of $\mathbf{E} \cdot \mathbf{B}$ in Fig. 13. Events with participant number between 130 and 140 are selected here (corresponding to an impact parameter around 8 fm) for Au+Au collisions at $\sqrt{s_{\text{NN}}} = 200 \text{ GeV}$. Results at two different locations, $(0, 3 \text{ fm}, 0)$

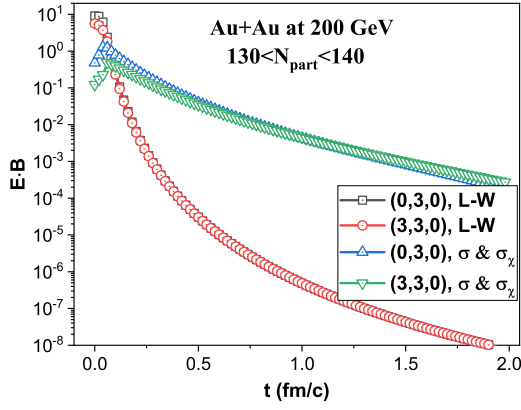


Figure 13. (Color online) The time evolution of $e^2 \mathbf{E} \cdot \mathbf{B}$ (in the unit of m_π^4) in 200 AGeV Au+Au collisions with $130 < N_{\text{part}} < 140$, compared between zero and finite conductivities, and two different locations.

and (3 fm, 3 fm, 0), are presented and compared between zero and finite conductivity scenarios. One can observe although the zero conductivity scenario starts with a larger $\mathbf{E} \cdot \mathbf{B}$ than the finite conductivity scenario, as has also been observed previously in Figs. 11 and 12, the former decays much faster than the latter. Therefore, including finite σ and σ_χ helps extend the influence of the electromagnetic field to a much later evolution stage of the QGP. Since stronger elliptic flow of the medium will be developed towards later time, introducing the electric and chiral magnetic conductivities may also quantitatively enhance the charge separation of v_2 , or the slope parameter r .

V. SUMMARY AND OUTLOOK

In this work, we have conducted a systematic study on the effects of the electric (σ) and chiral magnetic (σ_χ) conductivities on the spacetime evolution of the electromagnetic fields generated in high-energy nuclear collisions. By coupling the charge distribution from a MC Glauber model with the solution of the Maxwell equations that include both σ and σ_χ , or its zero conductivity limit (Lienard-Wiechert), we have calculated the time evolution of the spatial distributions of electric (\mathbf{E}) and magnetic (\mathbf{B}) fields, together with the electromagnetic anomaly ($\mathbf{E} \cdot \mathbf{B}$) and the electric quadrupole moment ($(\mathbf{E} \cdot \mathbf{B})\mathbf{B}$) at both zero and finite conductivities.

Our results show that although the electromagnetic field in vacuum is about an order of magnitude stronger than that in a conducting medium at the initial time, the former decays much faster than the latter. Additionally, in the transverse plane, while $|\mathbf{E}|$ and $|\mathbf{B}|$ appear symmetric about both $x = 0$ and $y = 0$ axes at zero conductivities, a broken symmetry about the $y = 0$ axis,

or the reaction plane, is observed after finite conductivities are introduced. This symmetry breaking is mainly from the non-vanishing azimuthal component with the presence of σ_χ for the electric field \mathbf{E}_T , while from the non-vanishing radial component with the presence of σ_χ for the magnetic field \mathbf{B}_T . The magnitudes of the longitudinal components of both \mathbf{E} and \mathbf{B} appear much smaller than their transverse component, while no symmetry breaking is observed for E_z and B_z after finite conductivities are introduced. A clear dipole structure for $\mathbf{E} \cdot \mathbf{B}$ and a quadrupole pattern for $(\mathbf{E} \cdot \mathbf{B})\mathbf{B}$ are still observed in our results although they are both distorted compared to the vacuum scenario due to the symmetry breaking of \mathbf{E} and \mathbf{B} fields in a conducting medium. Since the magnitude of \mathbf{E} decreases, while the magnitude of \mathbf{B} increases as the impact parameter increases, one can observe a non-monotonic dependence (first increase and then decrease) of $\mathbf{E} \cdot \mathbf{B}$ and $(\mathbf{E} \cdot \mathbf{B})\mathbf{B}$ with respect to the nucleon participant number in heavy-ion collisions. These dependences are found qualitatively consistent with the STAR data on the slope parameter r as a function of the participant number, indicating the QED anomaly could be an underlying mechanism that drives the v_2 separation between positive and negative charges. Since $(\mathbf{E} \cdot \mathbf{B})\mathbf{B}$ is more directly related to the electric quadrupole moment that gives rise to the charge separation, it appears to agree with the experimental data better than $\mathbf{E} \cdot \mathbf{B}$.

While this work provides a more quantitative understanding of the spacetime evolution of electromagnetic field and electromagnetic anomaly in relativistic heavy-ion collisions, it should be further improved in several directions. For instance, it is necessary to couple these profiles of electromagnetic field to hydrodynamic models or transport models for a more direct comparison to the charged particle observables, from which one may draw more solid conclusion about whether the QED anomaly is the key mechanism of the charge separation of the hadron v_2 . In addition, we assumed constant values of σ and σ_χ in the present study, which should vary as the QGP expands. Last but not least, apart from the slope parameter r of the v_2 separation, there exist other observables that may help place more stringent constraints on the electromagnetic field inside a conducting medium, such as the directed flow coefficient (v_1) of heavy quarks, whose precise theoretical description still remains a challenge with simplified modelings of the electromagnetic field in literature. We will extend our study to these aspects in our upcoming efforts.

ACKNOWLEDGMENTS

We are grateful to Xin-Li Sheng, Qun Wang and Xin-Li Zhao for very helpful discussions. This work was supported by the National Natural Science Foundation of China (NSFC) under Grant Nos. 12175122 and 2021-867.

-
- [1] Adam Bzdak and Vladimir Skokov. Event-by-event fluctuations of magnetic and electric fields in heavy ion collisions. *Phys. Lett. B*, 710:171–174, 2012.
- [2] Wei-Tian Deng and Xu-Guang Huang. Event-by-event generation of electromagnetic fields in heavy-ion collisions. *Phys. Rev. C*, 85:044907, 2012.
- [3] Jie Zhao, Hanlin Li, and Fuqiang Wang. Isolating the chiral magnetic effect from backgrounds by pair invariant mass. *Eur. Phys. J. C*, 79(2):168, 2019.
- [4] Yang Zhong, Chun-Bin Yang, Xu Cai, and Sheng-Qin Feng. A systematic study of magnetic field in Relativistic Heavy-ion Collisions in the RHIC and LHC energy regions. *Adv. High Energy Phys.*, 2014:193039, 2014.
- [5] D. E. Kharzeev, J. Liao, S. A. Voloshin, and G. Wang. Chiral magnetic and vortical effects in high-energy nuclear collisions—A status report. *Prog. Part. Nucl. Phys.*, 88:1–28, 2016.
- [6] D. Kharzeev and A. Zhitnitsky. Charge separation induced by P-odd bubbles in QCD matter. *Nucl. Phys. A*, 797:67–79, 2007.
- [7] Dmitri E. Kharzeev, Larry D. McLerran, and Harmen J. Warringa. The Effects of topological charge change in heavy ion collisions: ‘Event by event P and CP violation’. *Nucl. Phys. A*, 803:227–253, 2008.
- [8] Kenji Fukushima, Dmitri E. Kharzeev, and Harmen J. Warringa. The Chiral Magnetic Effect. *Phys. Rev. D*, 78:074033, 2008.
- [9] Jinfeng Liao. Anomalous transport effects and possible environmental symmetry ‘violation’ in heavy-ion collisions. *Pramana*, 84(5):901–926, 2015.
- [10] Xu-Guang Huang and Jinfeng Liao. Axial Current Generation from Electric Field: Chiral Electric Separation Effect. *Phys. Rev. Lett.*, 110(23):232302, 2013.
- [11] Umut Gürsoy, Dmitri Kharzeev, and Krishna Rajagopal. Magnetohydrodynamics, charged currents and directed flow in heavy ion collisions. *Phys. Rev. C*, 89(5):054905, 2014.
- [12] Umut Gürsoy, Dmitri Kharzeev, Eric Marcus, Krishna Rajagopal, and Chun Shen. Charge-dependent Flow Induced by Magnetic and Electric Fields in Heavy Ion Collisions. *Phys. Rev. C*, 98(5):055201, 2018.
- [13] S. Chatterjee and P. Bozek. Interplay of drag by hot matter and electromagnetic force on the directed flow of heavy quarks. *Phys. Lett. B*, 798:134955, 2019.
- [14] Gabriele Inghirami, Mark Mace, Yuji Hirono, Luca Del Zanna, Dmitri E. Kharzeev, and Marcus Bleicher. Magnetic fields in heavy ion collisions: flow and charge transport. *Eur. Phys. J. C*, 80(3):293, 2020.
- [15] Lucia Oliva. Electromagnetic fields and directed flow in large and small colliding systems at ultrarelativistic energies. *Eur. Phys. J. A*, 56(10):255, 2020.
- [16] Yifeng Sun, Vincenzo Greco, and Salvatore Plumari. The signature of charge dependent directed flow observables by electromagnetic fields in heavy ion collisions. *Eur. Phys. J. Plus*, 136(7):726, 2021.
- [17] Jun-Jie Zhang, Xin-Li Sheng, Shi Pu, Jian-Nan Chen, Guo-Liang Peng, Jian-Guo Wang, and Qun Wang. Charge-odd directed flows in heavy-ion collisions by Boltzmann-Maxwell equations. *arXiv:2201.06171*, 2022.
- [18] J. Adam et al. First Observation of the Directed Flow of D^0 and \bar{D}^0 in Au+Au Collisions at $\sqrt{s_{NN}} = 200$ GeV. *Phys. Rev. Lett.*, 123(16):162301, 2019.
- [19] S. Acharya et al. Probing the effects of strong electromagnetic fields with charge-dependent directed flow in Pb-Pb collisions at the LHC. *Phys. Rev. Lett.*, 125(2):022301, 2020.
- [20] Dam T. Son and Piotr Surowka. Hydrodynamics with Triangle Anomalies. *Phys. Rev. Lett.*, 103:191601, 2009.
- [21] Dmitri E. Kharzeev and Ho-Ung Yee. Chiral Magnetic Wave. *Phys. Rev. D*, 83:085007, 2011.
- [22] Yannis Burnier, Dmitri E. Kharzeev, Jinfeng Liao, and Ho-Ung Yee. Chiral magnetic wave at finite baryon density and the electric quadrupole moment of quark-gluon plasma in heavy ion collisions. *Phys. Rev. Lett.*, 107:052303, 2011.
- [23] Er-dong Guo and Shu Lin. Quark mass effect on axial charge dynamics. *Phys. Rev. D*, 93(10):105001, 2016.
- [24] Ioannis Iatrakis, Shu Lin, and Yi Yin. The anomalous transport of axial charge: topological vs non-topological fluctuations. *JHEP*, 09:030, 2015.
- [25] Max A. Metlitski and Ariel R. Zhitnitsky. Anomalous axion interactions and topological currents in dense matter. *Phys. Rev. D*, 72:045011, 2005.
- [26] D. T. Son and Ariel R. Zhitnitsky. Quantum anomalies in dense matter. *Phys. Rev. D*, 70:074018, 2004.
- [27] Dam Thanh Son and Naoki Yamamoto. Berry Curvature, Triangle Anomalies, and the Chiral Magnetic Effect in Fermi Liquids. *Phys. Rev. Lett.*, 109:181602, 2012.
- [28] M. A. Stephanov and Y. Yin. Chiral Kinetic Theory. *Phys. Rev. Lett.*, 109:162001, 2012.
- [29] Jian-Hua Gao, Zuo-Tang Liang, Shi Pu, Qun Wang, and Xin-Nian Wang. Chiral Anomaly and Local Polarization Effect from Quantum Kinetic Approach. *Phys. Rev. Lett.*, 109:232301, 2012.
- [30] Jiunn-Wei Chen, Shi Pu, Qun Wang, and Xin-Nian Wang. Berry Curvature and Four-Dimensional Monopoles in the Relativistic Chiral Kinetic Equation. *Phys. Rev. Lett.*, 110(26):262301, 2013.
- [31] Jiunn-Wei Chen, Jin-yi Pang, Shi Pu, and Qun Wang. Kinetic equations for massive Dirac fermions in electromagnetic field with non-Abelian Berry phase. *Phys. Rev. D*, 89(9):094003, 2014.
- [32] Jiunn-Wei Chen, Yen-Fu Liu, Shi Pu, Yu-Kun Song, and Qun Wang. Negative off-diagonal conductivities in a weakly coupled quark-gluon plasma at the leading-log order. *Phys. Rev. D*, 88(8):085039, 2013.
- [33] Daisuke Satow and Ho-Ung Yee. Chiral Magnetic Effect at Weak Coupling with Relaxation Dynamics. *Phys. Rev. D*, 90(1):014027, 2014.
- [34] Y. Burnier, D. E. Kharzeev, J. Liao, and H. U. Yee. From the chiral magnetic wave to the charge dependence of elliptic flow. *arXiv:1208.2537*, 2012.
- [35] Ho-Ung Yee and Yi Yin. Realistic Implementation of Chiral Magnetic Wave in Heavy Ion Collisions. *Phys. Rev. C*, 89(4):044909, 2014.
- [36] Guo-Liang Ma. Final state effects on charge asymmetry of pion elliptic flow in high-energy heavy-ion collisions. *Phys. Lett. B*, 735:383–386, 2014.
- [37] L. Adamczyk et al. Observation of charge asymmetry dependence of pion elliptic flow and the possible chiral magnetic wave in heavy-ion collisions. *Phys. Rev. Lett.*, 114(25):252302, 2015.

- [38] Xin-Li Zhao, Guo-Liang Ma, and Yu-Gang Ma. Novel mechanism for electric quadrupole moment generation in relativistic heavy-ion collisions. *Phys. Lett. B*, 792:413–418, 2019.
- [39] Mohamed Abdallah et al. Search for the chiral magnetic effect with isobar collisions at $\sqrt{s_{NN}}=200$ GeV by the STAR Collaboration at the BNL Relativistic Heavy Ion Collider. *Phys. Rev. C*, 105(1):014901, 2022.
- [40] Irfan Siddique, Xin-Li Sheng, and Qun Wang. Space-average electromagnetic fields and electromagnetic anomaly weighted by energy density in heavy-ion collisions. *Phys. Rev. C*, 104(3):034907, 2021.
- [41] Kirill Tuchin. Time and space dependence of the electromagnetic field in relativistic heavy-ion collisions. *Phys. Rev. C*, 88(2):024911, 2013.
- [42] Kirill Tuchin. Electromagnetic field and the chiral magnetic effect in the quark-gluon plasma. *Phys. Rev. C*, 91(6):064902, 2015.
- [43] Hui Li, Xin-li Sheng, and Qun Wang. Electromagnetic fields with electric and chiral magnetic conductivities in heavy ion collisions. *Phys. Rev. C*, 94(4):044903, 2016.
- [44] Yi Chen, Xin-Li Sheng, and Guo-Liang Ma. Electromagnetic fields from the extended Kharzeev-McLerran-Warringa model in relativistic heavy-ion collisions. *Nucl. Phys. A*, 1011:122199, 2021.
- [45] L. McLerran and V. Skokov. Comments About the Electromagnetic Field in Heavy-Ion Collisions. *Nucl. Phys. A*, 929:184–190, 2014.
- [46] Gabriele Inghirami, Luca Del Zanna, Andrea Beraudo, Mohsen Haddadi Moghaddam, Francesco Becattini, and Marcus Bleicher. Numerical magneto-hydrodynamics for relativistic nuclear collisions. *Eur. Phys. J. C*, 76(12):659, 2016.
- [47] John Blochynski, Xu-Guang Huang, Xilin Zhang, and Jinfeng Liao. Azimuthally fluctuating magnetic field and its impacts on observables in heavy-ion collisions. *Phys. Lett. B*, 718:1529–1535, 2013.
- [48] C. Loizides, J. Nagle, and P. Steinberg. Improved version of the PHOBOS Glauber Monte Carlo. *SoftwareX*, 1-2:13–18, 2015.
- [49] H. T. Ding, A. Francis, O. Kaczmarek, F. Karsch, E. Laermann, and W. Soeldner. Thermal dilepton rate and electrical conductivity: An analysis of vector current correlation functions in quenched lattice QCD. *Phys. Rev. D*, 83:034504, 2011.
- [50] Gert Aarts, Chris Allton, Alessandro Amato, Pietro Giudice, Simon Hands, and Jon-Ivar Skullerud. Electrical conductivity and charge diffusion in thermal QCD from the lattice. *JHEP*, 02:186, 2015.
- [51] Xin-Li Zhao, Yu-Gang Ma, and Guo-Liang Ma. Electromagnetic fields in small systems from a multiphase transport model. *Phys. Rev. C*, 97(2):024910, 2018.